Noble-free oxygen reduction reaction catalyst supported on Sengon wood (Paraserianthes falcataria L.) derived reduced graphene oxide for fuel cell application

Article *in* International Journal of Energy Research · December 2019

DOI: 10.1002/er.5015

CITATIONS
6

READS
67

8 authors, including:

Wulandhari Sudarsono
Universiti Kebangsaan Malaysia
8 PUBLICATIONS **11** CITATIONS
SEE PROFILE

Wai Yin Wong
Universiti Kebangsaan Malaysia
56 PUBLICATIONS **560** CITATIONS
SEE PROFILE

Kee Shyuan Loh
Universiti Kebangsaan Malaysia
98 PUBLICATIONS **1,353** CITATIONS
SEE PROFILE

Edy Herianto Majlan
Universiti Kebangsaan Malaysia
107 PUBLICATIONS **1,713** CITATIONS
SEE PROFILE

Received: 5 August 2019 | Revised: 23 October 2019 | Accepted: 6 November 2019

DOI: 10.1002/er.5015

RESEARCH ARTICLE

INTERNATIONAL JOURNAL OF ENERGY RESEARCH WILEY

Noble-free oxygen reduction reaction catalyst supported on Sengon wood (*Paraserianthes falcataria L.*) derived reduced graphene oxide for fuel cell application

Wulandhari Sudarsono[1] | **Wai Yin Wong**[1] | **Kee Shyuan Loh**[1] | **Edy Herianto Majlan**[1] | **Nirwan Syarif**[2] | **Kuan-Ying Kok**[3] | **Rozan Mohamad Yunus**[1] | **Kean Long Lim**[1]

[1]Fuel Cell Institute, Universiti Kebangsaan Malaysia, UKM, Bangi, Selangor, Malaysia

[2]Department of Chemistry, Universitas Sriwijaya, Jl. Palembang-Prabumulih km. 32, Inderalaya Sumsel, 30662, Indonesia

[3]Malaysian Nuclear Agency, Bangi, Kajang, Selangor, Malaysia

Correspondence
Wai Yin Wong Fuel Cell Institute, Universiti Kebangsaan Malaysia, 43600 UKM Bangi, Selangor, Malaysia.
Email: waiyin.wong@ukm.edu.my

Funding information
Universiti Kebangsaan Malaysia, Grant/Award Number: GUP-2018-013

Summary

Reduced graphene oxide (RGO) has progressed as one of key emerging carbon for catalyst support material. As an alternative to the conventional RGO precursor, biomass Sengon wood was converted into RGO for use as a noble metal free catalyst support in oxygen reduction reaction (ORR). This work intends to reveal the applicability of Sengon wood-derived RGO in anchoring/doping iron and nitrogen particles onto its surface and to study its ORR performance in a half-cell environment. Thin-sheet layer and highly defective (I_D/I_G) was gradually obtained at elevated pyrolysis temperature of Sengon wood graphene oxide (GO) at range 700°C to 900°C. As prepared RGO was further doped into catalyst (Fe/N/RGO) through the same pyrolysis procedure at a selected temperature after mixing the GO powder with iron chloride and different nitrogen precursors (urea, choline chloride, and polyaniline) at a fixed ratio. The ORR activity reached a current density up to 2.43 mA/cm^2, which in conjunction with smooth multilayer sheet morphology and high graphitic-N content as the active sites. Stability analysis indicated an 85% current efficiency and only 0.03-V reduction in onset potential on methanol resistant test for Fe/ChoCl/RGO catalyst. This study revealed that Sengon wood-derived RGO successfully supported Fe-N-C catalyst which showed comparable oxygen reduction activity to Pt/C.

KEYWORDS

catalyst support, ORR activity, reduced graphene oxide, Sengon wood

1 | INTRODUCTION

Carbon support is one of the key determining factors for catalyst performance in various electrochemical applications, such as metal-air batteries and fuel cells.[1,2] The carbon structure has a strong influence on the anchoring effect of metal and auxiliary atoms on its surface, which is crucial in providing fixed reaction sites for the reactants.[3] Various types of carbons, such as carbon black,[4] multiwall carbon nanotubes (MWCNTs),[5] activated carbon,[6] C/polymer composite,[7] and graphene, have been identified as key potential catalyst support materials in fuel cells. The use of carbon nanostructures was shown to significantly increase the current density, durability, and stability of the electrode due to the increase in the specific surface area and a strong anchoring effect. Among all materials, graphene has drawn the most interest due to its ability to prevent the agglomeration of metal species to increase the stability and mass transport on the electrode.[8] Nonetheless, graphene production faces problems related to synthesis cost, method preparation, and production from nonrenewable

graphite sources. In view of the substantial potential of graphene as a catalyst support, there is a need to look for alternative renewable sources using biomass as a substitution. Sengon wood, which originates in Indonesia, is widely harvested for light wood building construction. Leftover branches and trunk have the potential to gain added value as biomass sources. Interestingly, Sengon wood was enriched by cellulose, hemicellulose, and lignin previously observed to construct a defective honeycomb structure and high oxygen content. This structure has the potential to be further processed into graphene-like carbon via chemical treatment.[9,10]

Currently, biomass-derived graphene is extensively prepared via a base activation method with high-temperature pyrolysis. Indeed, this method has successfully produced multilayer graphene from various biomass sources such as peanut shell,[11] populus wood,[12] spruce bark,[13] and wheat straw.[14] Physical characterization showed a stacked multilayer nanosheet and six less well-defined rings, which still lead to the argument for the formation of either graphite, graphene, or activated carbon structures.

Attempts have been made to successfully apply biomass graphene to various electrochemical applications due to its high surface area, high conductivity, and many active sites for catalytic activity. For electrochemical storage applications, the resultant capacitance and surface area of biomass carbon are comparable to those of existing commercial carbon sources. Nonetheless, there has yet to be any standard procedure and reference to the synthesis of graphene-like structures from biomass carbon despite the success of the base activation method. In addition, there have yet to be works to explore different methods for such synthesis, and this provides us with an opportunity to venture into the use of the Hummer's method, which is conventionally used to produce graphene oxide (GO) and can be used to further pyrolyze and reduce to produce reduced graphene oxide (RGO) as the graphene family from graphite. This method can be conveniently used to produce rich functionality and well-dispersed RGO (a family of graphene), and such properties are desired as catalyst supports.[15] The intermediate oxidation stage of biomass can create defective sites, which upon further reduction can be turned into active sites to anchor the catalysts more strongly onto the surface.[16] Thus, we expected that the biomass RGO synthesized via the Hummer's method would be able to serve as a strong and active catalyst support for electrocatalysts. Considering the fast-growing works on noble-metal-free iron/nitrogen/carbon (Fe-N-C) catalysts as the highest potential low-cost oxygen reduction reaction (ORR) catalysts for fuel cell applications, this work will attempt to anchor various Fe-N-C with different nitrogen precursors such as urea, polyaniline, and choline chloride onto the biomass RGO support. The use of the biomass RGO is expected to result in comparable (ORR) activity under alkaline conditions as reported Fe-N-C catalysts.[17]

Herein, we report for the first time the conversion of biomass into RGO via the Hummer's reduction method and its application as a catalyst support for fuel cell ORRs at the cathode. In this work, biomass RGO was initially synthesized at different pyrolysis temperatures after the Hummer's reduction process, and the structure of the RGO obtained was examined. The pyrolysis temperature was selected for the synthesis of the catalyst in a one-pot thermal treatment with iron chloride salt and nitrogen precursors to obtain Fe/X/RGO (X = nitrogen precursor) on biomass RGO and was followed by characterization to determine the ORR activity of the noble-free catalysts supported on biomass RGO.

2 | MATERIALS AND METHOD

2.1 | Material preparation

2.1.1 | RGO preparation

Sengon wood biomass was initially ground and crushed into particles sized 0.1 mm with an ultra-centrifugal mill. The raw Sengon wood powder was hydrothermally processed to remove the lignin content at 200°C for 16 hours.[18] Next, carbonisation was done by microwave heating (Sharp R125IN, 800 W) for 25 minutes. The obtained black carbon powder was purified and then further subjected to the Hummer's method to produce GO. Briefly, 3 g of Sengon wood carbon powder and 3 g of sodium nitrate (R&M chemical, 99% A. R Grade) were added to 100-mL 95% to 98% sulfuric acid (Systerm, 95-98% AR Grade). The mixture was stirred for 1 hour in an ice bath. Next, 9 g of $KMnO_4$ (R&M Chemical, 99% ChemPure) was gradually added. The reaction was kept at 20°C for an hour and then stirred continuously at room temperature (±35°C) for 24 hours until a brown paste was formed. Then, 100-mL deionized water was added to the solution, followed by continuous stirring for another 24 hours. Subsequently, 10 mL of hydrogen peroxide (Systerm, 30% ChemAr) was added to the mixture to terminate the oxidation process along with the addition of 100-mL DI water with stirring for another 2 hours. The suspension was filtered and washed alternately with 5% hydrochloric acid and deionized water using centrifugation. The obtained black precipitate was exfoliated to GO through sonication for 30 minutes and dried at 80°C overnight. The GO was then subjected to pyrolysis at three different temperatures (700°C, 800°C, and 900°C)[19] for 1 hour under inert conditions to obtain RGO 700, RGO 800, and RGO 900, respectively, and was kept prior to characterization. For the preparation of Fe/X/RGO catalysts on biomass RGO, the as-produced GO was used to mix with the catalyst precursors via the following procedure. As a control, RGO from graphite (RGO graphite) was prepared following the same procedure.

2.1.2 | Catalyst preparation

In this work, the initial chemical synthesis methods of Fe/X/RGO catalysts from various nitrogen precursors were different due to their different chemical nature. Nonetheless, the ratio of iron chloride ($FeCl_3$) and RGO was kept at 2:5 by weight ratio, while the pyrolysis temperature was fixed at 900°C after the first evaluation of the properties of the biomass RGO.[20] An acid wash with 0.5 M sulfuric acid for 6 hours was performed on the as-produced Fe-N-C to remove any metal residues on the catalyst surface.

2.1.3 | Fe/Urea/RGO

The prepared GO was diluted in 30 mL of DI water (milipore, 18.2 mΩ/cm) with 2 mmol of $FeCl_3$ (Systerm, ChemPur) and urea (Systerm, chemAr 99%) at a ratio of 2:5. The mixture was stirred for 1 hour followed by sonication for 30 minutes. The homogenized mixture was placed into a 150-mL Teflon-lined autoclave and heated in an oven at 190°C for 8 hours. The hydrothermal reaction aimed to create a crystalline composite of catalyst. The resulting black solution was further dried at 80°C and then pyrolyzed at the optimal RGO pyrolysis temperature.

2.1.4 | Fe/ChoCl/RGO

$FeCl_3$ and ChoCl (Acros organic, AR 99%) were mixed and continuously stirred in a hot water bath at 80°C under inert conditions until a yellowish solution was formed.[21] Subsequently, 0.8 g of GO was added into solution and continuously stirred until a homogeneous mixture was obtained. The resulting powder was further processed via pyrolysis and acid wash as mentioned above.

2.1.5 | Fe/Pani/RGO

$FeCl_3$ and GO with respective ratios were mixed in 30-mL 0.5 M HCl under water bath conditions. Subsequently, 2-mL aniline (Acros organic 99%, ACS Reagent) was added into the solution, followed by the oxidant salt and ammonium persulfate (Systerm, 99% ChemAr) at a molar ratio of 1:1. The mixture was stirred for 24 hours to obtain a viscous dark green suspension.[22] The solvent was evaporated and oven dried prior to pyrolysis and washing.

2.2 | Physicochemical and electrochemical characterizations

Raman spectroscopy (Invia Qontor Renishaw) with a 532-nm wavelength detector at 50 keV was employed to confirm the success of RGO production from Sengon wood biomass. X-ray diffraction (XRD) (Panalytical, X'pert Pro MPD PW 3040/60) with a scanning rate of 30 step/second was used to investigate the crystallinity and compliment the Raman spectra for confirmation of RGO production. The scanning was performed at a wide angle in the range of $2\theta = 5°$ to 80°. A field emission scanning electron microscope (FESEM) (Carl Zeiss, GeminiSEM 500) with secondary electron scattering at a magnification of 20 kV was used to investigate the surface morphology of the biomass RGO and catalyst samples. TEM Thermo Fisher Model: Talos 120C, was used to examine the success of RGO produced from the Sengon wood. The RGO and catalyst samples' surface area and pore analysis were performed using Brunauer, Emmett, Teller (BET) analyser (Micromeritics 3Flex). N_2 adsorption was performed at 77 K with gradual desorption at temperatures of 30°C, 90°C, and 120°C for every 30 minutes in 8-hour duration. X-ray photoelectron spectroscopy (XPS) was performed at Synchotron Beamline 3.2Ua with Al Kα radiation in the scan range of 200 to 1200 eV. All spectra were fitted with a Shirley background and calibrated to the respective C 1s reference of 284.8 eV (binding energy shifted for less than 1 eV).

For electrochemical characterization, a catalyst ink was prepared using 5-mg catalyst, a mixture of ethanol and DI water (3:1), and 50-μL 5 wt% Nafion ionomer solution. The mixture was dispersed in an ultrasonic sonicator for 1 hour to obtain a homogeneous mixture. Next, 10 μL of catalyst was deposited on a rotating-ring disk electrode (RRDE) from Pine Instrument, Inc. and left overnight for drying prior to testing.[23] Cyclic voltammetry (CV) was performed with a negative scan through a potential window from −0.9 to 0.1 V vs Ag/AgCl (3 M, Metrohm) using a three-electrode system (half-cell reaction) in which a 5-mm-diameter glassy carbon electrode (Pine Research Instrument Inc.), Ag/AgCl electrode, and platinum wire served as the working, reference, and counter electrodes, respectively. All measurements were conducted using Autolab PGSTAT128N with 0.1 M KOH electrolyte via a scan rate of 10 mV/s in a N_2- and O_2-saturated environment. Rotating disk voltammetry (RDE) was performed to obtain the electron transfer number of the catalyst. The working electrode was subjected to rotation at 200 to 1600 rpm under an O_2-saturated environment. The recorded potential was converted into reversible hydrogen electrode (RHE) with $V_{RHE} = V_{Ag/AgCl} + 0.9654$ V. Koutecky-Levich plots were produced using Equation (1).[24]

$$\frac{1}{j} = \frac{1}{j_k} + \frac{1}{j_l} = \frac{1}{j_k} + \frac{1}{0.62nFAC_o^* D_o^{2/3} v^{-1/6} \omega^{1/2}} \quad (1)$$

where j_k, j_l, and j are the kinetic current density, limiting diffusion current density, and current density, respectively, n is the number of electrons, C_o is the O_2 concentration in 0.1 M KOH (1.26×10^{-6} mol/cm^3), D_o is O_2 diffusivity in 0.1 M KOH (1.93×10^{-5} cm^2/s), v is the kinetic viscosity of the solution (0.01 cm^2/s), and ω is the rotation speed in rpm. $1/j$ vs $1/\omega^{1/2}$ was plotted to obtain the electron transfer number. For the RRDE calculation, n and the peroxide yield were calculated using the following equations (2) and (3),[24] with I_d, I_r, and N are disk current, ring current, and ring-disk electrode coefficient (N is calculated as 0.37)

$$n = \frac{4I_d}{I_d + \frac{I_r}{N}} \quad (2)$$

$$\%H_2O_2 = \frac{\frac{I_r}{N}}{I_d + \frac{I_r}{N}} x\,200\% \quad (3)$$

The kinetic parameters for oxygen reduction were obtained using Equation (4),[25] obtained from the RDE data.

$$\eta = a\log j_o - b\log j_k \quad (4)$$

where η is the thermodynamic overpotential, j_k is the kinetic current density (mA/cm^2), b is Tafel slope (mV/dec), a is constant, and j_o is the

exchange current density (mA/cm^2). The transfer coefficient, α, was derived FROM Tafel slope using Equation (5)[25,26]:

$$b = -\frac{2.303RT}{\propto nF} \quad (5)$$

where R is the gas constant (8.314 J/K.mol), *T* is operating temperature (K), and F is Faraday's constant (96 485 C/mol). Stability was conducted using chronoamperometry technique with working electrode rotated at 1600 rpm in O_2-saturated environment for 16 000 seconds. Methanol tolerance study was conducted using the RDE technique at 1600 rpm, with the addition of 6 mL of 3.0 M methanol to O_2-saturated 0.1 M KOH solution to observe the changes on polarisation curve before and after the addition.

3 | RESULTS AND DISCUSSION

The Raman spectra in **Figure 1A** show two characteristic peaks at 1300 and 1590 cm^{-1} for all samples, which are the D and G bands, respectively. The D band indicates defect sites due to the effect of edge sheet disruption, while the G band indicates the graphitic planar sp^2 bond.[27] Each temperature of biomass RGO had a lower I_D/I_G ratio than the RGO from graphite, which also confirmed the formation of a less defective graphene material. The I_D/I_G ratios were 0.848, 0.866, and 0.92 for RGO 700, RGO 800, and RGO 900, respectively, while RGO graphite was I_D/I_G = 1.05. The increase in pyrolysis temperature to produce the biomass RGO has increased the number of defective sites on RGO. This is attributed to the effect of heat treatment at higher temperature through pyrolysis that has removed greater amount of oxygen-containing groups and caused a breakage on sp^2 bond in graphene layers into sp^3 bond, leading to higher vacancy defects on the surface.[28,29] The success of the synthesis of RGO was further confirmed by the XRD spectra in **Figure 1B.** The diffraction peaks at 2θ values of 25° to 26° and 44°, which correspond to the (002) and (100) planes, respectively, confirmed the formation of RGO, and the lack of peak at 10° indicated that the GO was reduced to RGO for all samples. In comparison to the pure graphene sample, broader peaks were observed for the RGO 700, RGO 800, and RGO 900 samples due to the disruption from the oxygen group on the sp^2 carbon lattice during the reduction process, which created a less crystalline structure in the biomass RGO samples.[30] RGO 900 had a smaller peak shift relative to pure graphene for the (002) plane from 2θ = 25.89° to 26.48°, compared with RGO 700 (2θ = 26.52°) and RGO 800 (2θ = 26.5°), thus indicating a similar lattice structure with that of the benchmark. This result further confirms that a higher pyrolysis temperature is beneficial in removing the oxygen-containing group on the surface, resulting in increased crystal structure distortion. Furthermore, prominent peaks at 2θ = 44° on both RGO corresponded to the distortion force between graphene layers,[31] and hence, these observations confirmed the formation of RGO from Sengon wood biomass.

The morphology of the biomass RGO was investigated in the FESEM micrographs as shown in **Figure 2**. **Figure 2A** shows that for pyrolysis at 700°C, the produced RGO was a bulky thick layer, and it was suspected that the carbon layers were not completely exfoliated. In contrast, at a higher pyrolysis temperature of 800°C, the layer began to be transparent, which initially demonstrated that the graphene layer started to peel off (as shown in **Figure 2B**). **Figure 2C** shows thin nanosheet layers that were observed more vividly at 900°C, which confirms the exfoliated graphene layers on the Sengon biomass.[13] Further TEM characterization shown in **Figure 2D,E** identified thin and transparent layers with defined spots and ring on selected area electron diffraction (SAED) data had indicated the lattice fridge on RGO, and thereby supporting successful RGO formation from Sengon wood.[31] Interestingly, the BET N_2 adsorption and desorption demonstrate a higher surface area on RGO 900 (405.16 m^2/g) than RGO from graphite (372.6 m^2/g) sources. This is believed to be beneficial for the RGO from Sengon wood to serve as a catalyst support.

Nonetheless, overall, compared with the RGO prepared from graphite, the RGO from Sengon wood was merely multilayer RGO, which has yet to be achieved as high quality graphene-based material. The agglomeration on RGO layer was prompt by the incomplete mechanical exfoliation due to the re-stacking of sp^3 bond on graphene lattice.[32,33] Although the mechanism of the synthesis of RGO from biomass sources is still vague and requires more comprehensive and systematic study. However, we postulate that the reduction process follows steps similar to those from graphite sources. Bulky vessel-like biomass carbon undergoes a harsh acid treatment that exfoliates the

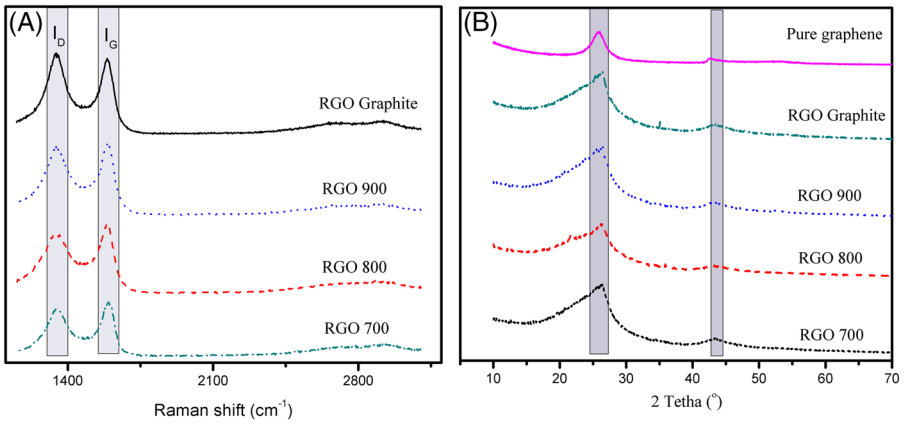

FIGURE 1 (A) Raman spectra of RGO; (B) XRD spectra of RGO and graphene as reference

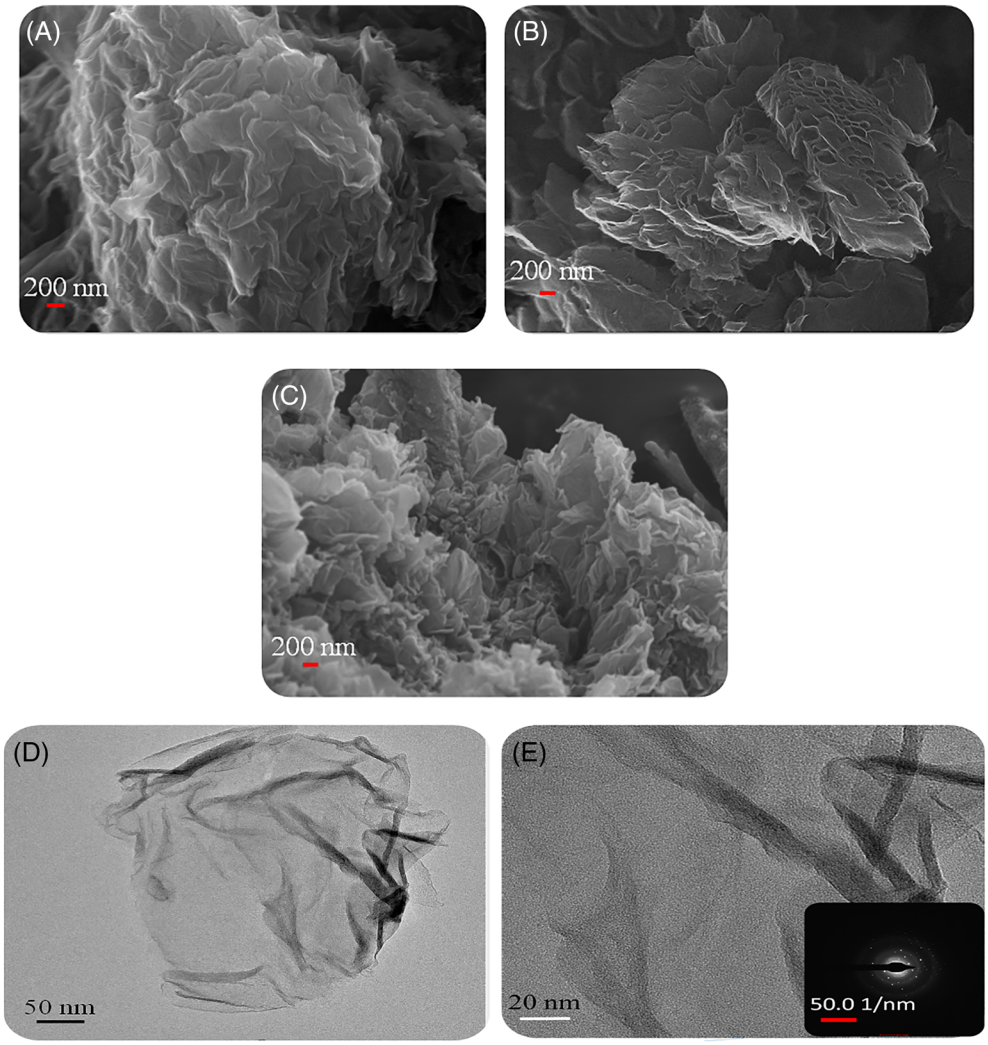

FIGURE 2 SEM image for (A) RGO 700, (B) RGO 800, (C) RGO 900 and TEM imaging of RGO 900 (D-E)

layers into carbon nanosheets. Some of the oxidants were able to intercalate inside the nanosheet layer and form an oxygen group and hence enlarge the space between the layers. In our case, biomass was converted into GO through the Hummer's method. Biomass carbon was oxidized with harsh treatment using dipermanganate heptaoxide (Mn_2O_7). This species was intercalated into the biomass carbon layer with functionalized oxygen groups among the layers.[34,35] The ratio of oxygen functionalities must be controlled to provide vacancies or sites for anchoring auxiliary metals or atoms. As concluded from the characterization, pyrolysis at 900°C resulted in RGO with many defect sites, few oxygen-containing groups, sheet-like morphology, and high graphitization, and thus, this was selected as the fixed temperature for catalyst preparation.

For catalyst preparation, the GO intermediate was used as the precursor with iron chloride and nitrogen precursors. The oxygen-rich surface in GO leads to an increase in hydrophilic properties that facilitate dispersion in DI water. Therefore, the simultaneous reduction of GO and metal nanoparticles would prevent the restacking and self-agglomeration of edge graphene particles.[36] During the one-pot synthesis at a fixed pyrolysis temperature of 900°C, metal can anchor on the defect sites of GO while removing the oxygen group from the surface, thus producing Fe/X/RGO (X = ChoCl, Urea, Pani). **Figure 3** shows the CV curve of the as-produced Fe/X/RGO catalysts with different nitrogen precursors and the control samples of RGO 700, RGO 800, and RGO 900. The reduction peak was absent for RGO 700 pyrolysed at lower temperature; while only a small reduction peak was observed on RGO 800 at 0.55 V vs RHE. These phenomena were related to the smaller number of edge defect sites at lower pyrolysis temperatures, which serve as the active sites for oxygen reduction.[37] Obviously, the depleted of reduction peaks was occurred on RGO 800, apparently due to insufficient distribution of oxygen removal disperse on RGO surface.[38,39] RGO 900 exhibited some ORR activity with a low onset potential at 0.77 V, which is possibly attributed to success formation of thin nanosheet RGO layers with large surface defects upon the removal of oxygen groups on the carbon matrix.[40]

Interestingly, it was observed that the capacitive current was depleted in the presence of metal and nitrogen atoms on RGO, which was likely due to the effect of atomic metal anchorage on the RGO defect sites. Generally, the onset potential and peak reduction of the catalyst were increased relative to those of former RGO, yet they indicate a synergetic effect from iron and nitrogen incorporating onto the surface. Among the three different nitrogen precursors, screening via CV demonstrated that Fe/ChoCl/RGO exhibited the highest reduction peak potential at 0.785 V with an onset potential at 0.88 V,

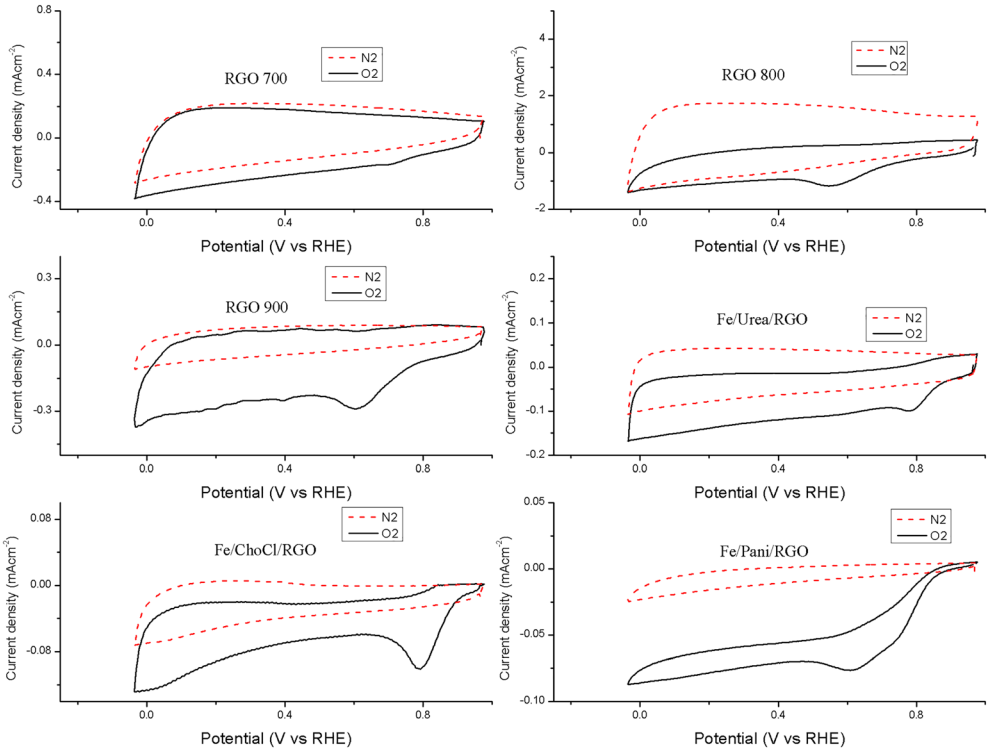

FIGURE 3 Cyclic voltammogram of Fe/X/RGO, RGO 700, and RGO 900 catalysts in 0.1 KOH electrolyte under nitrogen-saturated (red lines) and oxygen-saturated (black lines) conditions

indicating better ORR activity with the lowest overpotential. Fe/Urea/RGO and Fe/Pani/RGO followed with lower onset potentials of 0.87 and 0.83 V, respectively. In conjunction with the CV results, the XPS surface analysis detected a contribution from the iron content to the CV reduction peaks. As shown in Table 1, the iron metal content from the surface scan was 2.39, 4.86, and 1.41 wt% for Fe/Urea/RGO, Fe/ChoCl/RGO, and Fe/Pani/RGO, respectively. Fe/ChoCl/RGO showed the highest iron content, which agrees with the aforementioned oxygen reduction peaks on the CV scan. Meanwhile, Fe/Pani/RGO with the lowest iron content showed to exhibit the lowest reduction potential value, correlate with its inferior ORR activity compared with other Fe/X/RGO catalysts (**Figure 3**). Therefore, iron metal plays an important role in contributing to the active sites on ORR catalysts.

The ORR activity of the catalysts was further studied via rotating disk voltammetry that eliminated the mass diffusion factor. As shown in **Figure 4**, the onset potential of each catalyst was 0.89, 0.91 V and 0.87 V vs RHE for Fe/Urea/RGO, Fe/ChoCl/RGO, and Fe/Pani/RGO, respectively, which agreed with the CV results. Nonetheless, these values were slightly lower than those of the commercial Pt/C catalyst, which is 0.97 V due to the small *d* band gap and few vacancies on the atomic transition state of Pt. The positive shift in the onset from 0.805 V with RGO 900 for all catalysts indicated that Fe metal and nitrogen play vital roles in creating active sites for ORR activity.[41,42] The half wave potential was another parameter for determining the ORR activity of each catalyst. The values of the half wave potentials ranged from 0.66 to 0.79 V. Among all, Fe/ChoCl/RGO achieved the highest half wave potential at 0.84 V, and the difference from Pt/C ($\Delta E_{1/2}$) was only −56.1 mV, which was considerably small, indicating its potential as an active ORR catalyst. RGO 900 shows much lower onset potentials and the absence of a limiting current density at potentials below 0.5 V, which indicates insufficient and unevenly distributed active sites on the defective carbon surface.[26] Furthermore, this confirms that RGO SW has similar kinetic properties as oxidized graphene, as previously reported by Jiao and his coworker.[43]

Apart from kinetic region, the ORR in the potential range < 0.5 V vs RHE was apparently controlled by mass transport diffusion. As depicted in **Figure 4**, Fe/Pani/RGO did not achieve the limiting plateau owing to the poor distribution of active sites that have interfered the mass transport. Meanwhile, both Fe/ChoCl/RGO and Fe/Urea/RGO achieved a quasi-limiting plateau, indicating a better active site distribution on the catalyst surface. The current densities were described at pointed potential 0.12 V vs RHE with significant increase in the order of Fe/Pani/RGO (2.084 mA/cm^2), Fe/Urea/RGO (2.22 mA/cm^2), and Fe/ChoCl/RGO (2.43 mA/cm^2) which are correlated to the surface morphology of the catalysts. **Figure 5A** demonstrates that the Fe/Urea/RGO catalysts in the form of crumpled agglomerates decorate the surface of the RGO sheets. Fe/ChoCl/RGO **(Figure 5B)** is a smooth multilayered sheet with some coarse particles deposited on the surface without any agglomerates. In contrast, Fe/Pani/RGO in **Figure 5C** has catalyst particles that appeared as dense, rough, and amorphous layers, which are suspected to cover the entire surface of RGO. This coverage is likely attributed to the polymer nature of Pani, which formed large agglomerates due to incomplete reduction of GO that decreased the number of nitrogen atoms doped on the carbon surface. In addition, it is worth noting that the one-step pyrolysis with a shorter period than a two-step pyrolysis that was adopted to synthesize Fe/Pani/RGO may have resulted in the formation of agglomerates.[44]

TABLE 1 ORR activity and elemental composition from XPS spectra

Samples	V_{onset} (V vs RHE)	$E_{1/2}$ (V vs RHE)	J ($mAcm^{-2}$)	Fe (at%)	C (at%)	O (at%)	N (at%)	Fe 2p (at%)				N 1s (at%)		
								$Fe^{2+}_{3/2}$ (710 ± 1 eV)	$Fe^{2+}_{1/2}$ (723 ± 1 eV)	$Fe^{3+}_{3/2}$ (713±1 eV)	$Fe^{3+}_{1/2}$ (725±1 eV)	Pyridinic N (398 ± 1 eV)	Pyrrolic N (400 ± 1 eV)	Graphitic N (401 ± 1 eV)
RGO 900	0.80	0.74	1.8				-					-	-	-
Fe-Urea-RGO	0.89	0.81	2.22	2.39	71.89	23.37	2.36	1.08	0.46	0.35	0.18	0.92	0.68	0.75
Fe-ChoCl-RGO	0.91	0.84	2.43	4.86	79.64	11.53	3.97	1.79	0.88	1.05	0.64	0.71	0.21	3.05
Fe-Pani-RGO	0.87	0.70	2.084	1.41	50.62	30.69	17.29	0.27	0.33	0.43	0.16	7.20	9.60	0.49
Pt/C	0.97	0.87	3.21	-	-	-	-					-	-	-

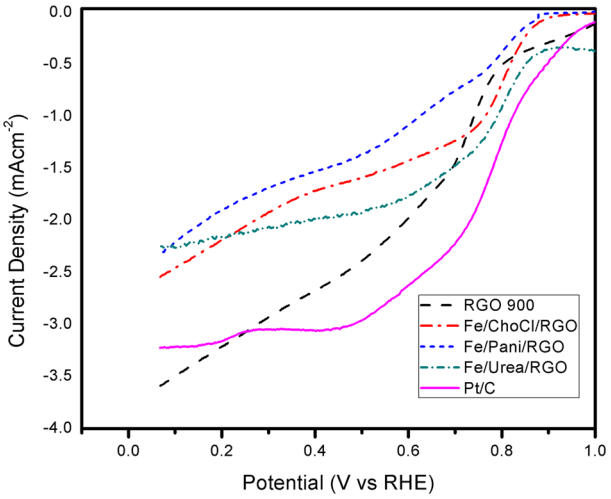

FIGURE 4 Linear swept voltammograms of all catalysts, RGO and Pt/C at 1600 rpm under O_2-saturated condition in 0.1 M KOH electrolyte

Further kinetic analysis to determine the ORR mechanism on the catalyst was performed through Tafel slope calculation in the kinetic control region. The Tafel slopes at low current density (lcd) region (0.9-0.8 V vs RHE) were measured as 189 mV/dec for Fe/Urea/RGO, 81 mV/dec for Fe/ChoCl/RGO, and 109 mV/dec for Fe/Pani/RGO. As compared with the benchmark value of 60 mV/dec on Pt/C, it is worth noting that only Fe/ChoCl/RGO showed the nearest value, implying that this catalyst would follow a one electron transfer as the rate-determining step, similar to that on Pt/C. The kinetic and mass transport parameter were crucial factors on determining the utilisation of catalyst in further application, and thereby, we postulate that Fe/ChoCl/RGO as the most active Fe-N-C catalyst in this work to catalyse the ORR in alkaline media.

The highest activity as observed in Fe/ChoCl/RGO compared with other catalysts can be correlated to the morphology and its elemental composition. During the catalyst synthesis of Fe/ChoCl/RGO, it was believed that choline chloride as the organic salt that is highly miscible in water was able to penetrate through the Sengon wood GO during the mixing. Upon pyrolysis, the organic salt containing nitrogen was embedded and possibly doped into the RGO matrix, leaving solely iron particles from the iron salt precursor to anchor on the RGO surface. This work shows good agreement with that of Mondal and his coworker,[21] who used *Sargassum tenerrimum*, seaweed biomass, and a deep eutectic solvent of ChoCl:$FeCl_3$ to synthesize Fe-functionalized graphene for an ORR study. Similar morphologies with Fe particles were observed on the functionalized graphene with the N dopant detected in the catalyst without the appearance of large particle agglomeration. The catalyst was reported to demonstrate a 0.83-V onset potential and 0.78-V half wave potential in a similar electrolyte environment, and our current work presents better ORR activity in the kinetic region. This difference could be attributed to the RGO used in this study, which has more active sites. In addition, catalysts that exist in the form of graphene sheet-*like* structures are well known to be more chemically active under alkaline conditions for the ORR,

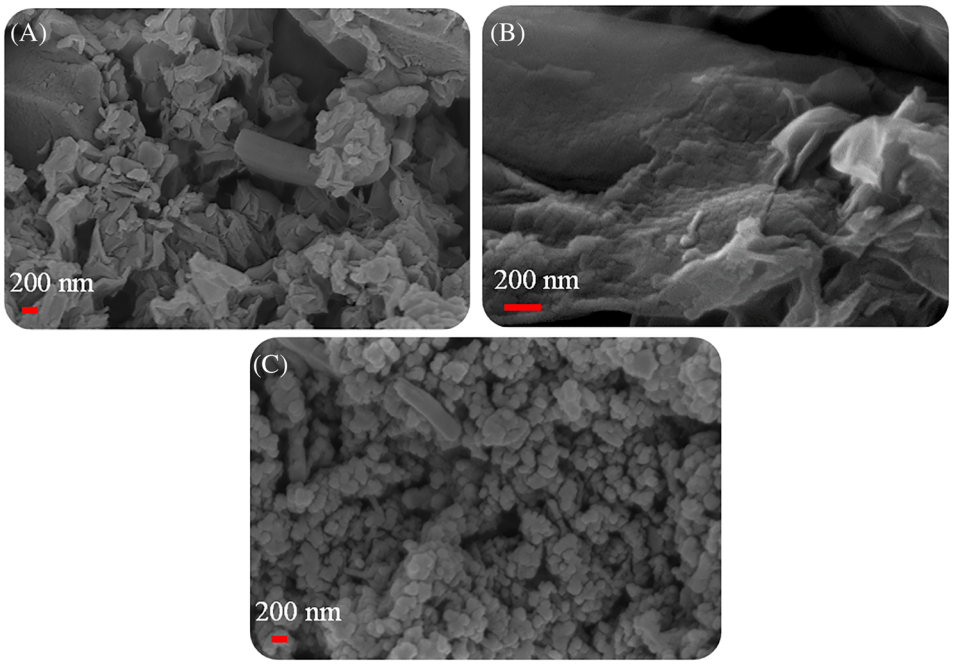

FIGURE 5 SEM images of (A) Fe/Urea/RGO, (B) Fe/ChoCl/RGO, and (C) Fe/Pani/RGO

and the catalytic activity is predicted to occur at the edge of the RGO layers.[36] It is also evident that the dense and amorphous Fe/Pani/RGO has the lowest onset potential that reflects its poor ORR activity. This can also be correlated with the nitrogen bonding states on the catalyst surface that will be discussed later. In addition to the morphology, the type of nitrogen doped on the surface might affect the limiting current. Based on Table 1, the higher number of graphitic N on both Fe/ChoCl/RGO and Fe/Urea/RGO synergistically increased the limiting current density on the catalyst.

To further explain the ORR activity based on the structural and chemical properties of the catalysts, XRD spectra are presented in **Figure 6**. The spectra demonstrate that all catalysts showed the presence of the characteristic peaks of RGO at 2θ = 26° and 43° despite the sharpness of the peaks being different. This result confirmed that the

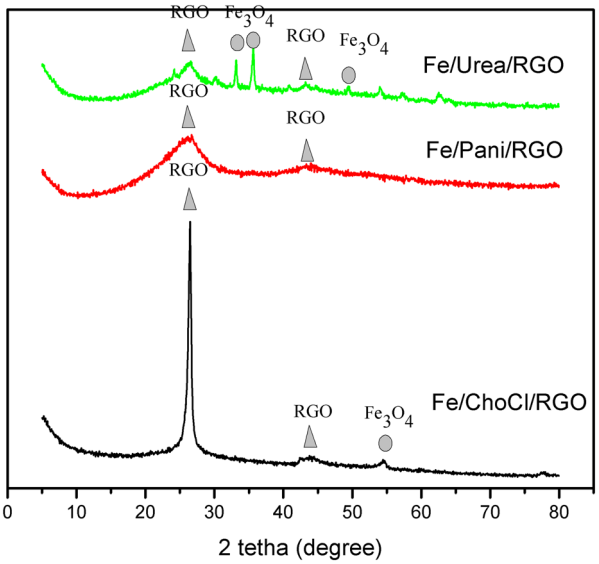

FIGURE 6 XRD spectra of Fe/X/RGO (X = Urea, Pani, and ChoCl)

one-pot thermal treatment successfully reduced GO to RGO. Interestingly, Fe/ChoCl/RGO showed a sharp peak at 2θ = 26°, implying the formation of a high crystalline multilayer graphene-sheet layers on the catalyst, which is evident from the micrograph in **Figure 5B.**[21] Furthermore, the peak at 2θ = 54° confirmed the existence of Fe_3O_4. The XRD spectra for Fe/Urea/RGO showed extra peaks at 35.02° and 57°, corresponding to the presence of Fe_3O_4 (ICSD no. 98-001-2141). The broader peak observed at 2θ = 26°, indicating a more amorphous form of carbon, corresponds to the formation of catalyst agglomerates on the thin sheets of RGO from Sengon wood biomass. For Fe/Pani/RGO, the amorphous phase of carbon was dominant without the appearance of Fe peaks. This is possibly due to the formation of the dense agglomerate that was explained earlier as the major constituents of carbon. Hence, we can confirm herein with the SEM images that the graphene sheet-*like* structure is more favourable for ORR activity in alkaline media. In addition, the presence of iron was shown to have a positive contribution to the ORR activity, which can be observed in the much higher onset and half wave potential of the Fe/ChoCl/RGO and Fe/Urea/RGO catalysts.

Figure 7A demonstrates N_2 absorption/desorption in isotherm linear plot. At high relative pressure (>0.05), Fe/Urea/RGO and Fe/ChoCl/RGO exhibited a steep increment on absorption peaks, attributed to type IV isotherm plot, hysteresis loop type 4 (H4). This indicated the existence of large mesopore number on catalysts.[45] In contrast, Fe/Pani/RGO displayed a reversible loop on the isotherm plot, categorized as type II isotherm. This isotherm plot inferred the absence of micro/mesopores on Fe/Pani/RGO, in good agreement with its surface morphology that showed dense agglomeration, that has disrupted the growth of interspace voids.[46] The BET surface area of the catalysts were 249.18, 55.15, and 19.58 m^2/g and total pore volume 0.19, 0.186, and 0.11 cm^3/g for Fe/Urea/RGO, Fe/ChoCl/RGO, and Fe/Pani/RGO, respectively. From above data, the Fe/Urea/RGO and Fe/ChoCl/RGO demonstrated analogous pore

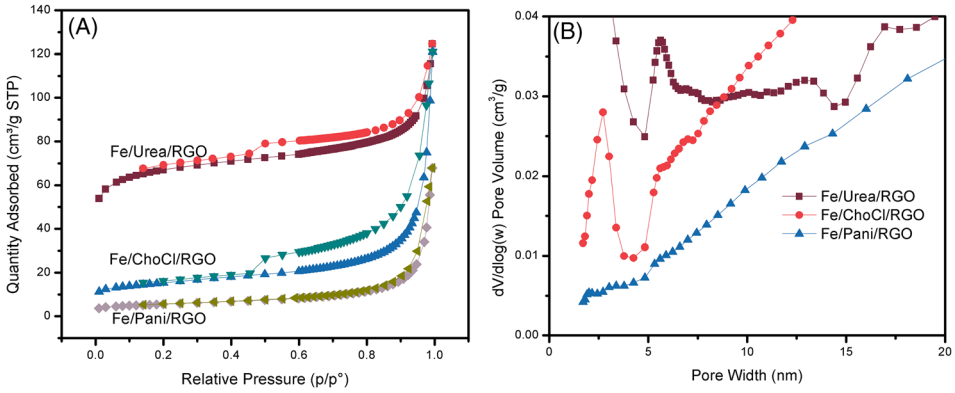

FIGURE 7 (A) BET adsorption/desorption at nitrogen 77 K; (B) pore distribution size on Fe/X/RGO (X = Urea, ChoCl,and Pani)

volume size despite the differences in the surface area. High pore volume was believed to accelerate the oxygen reactants to arrive at the active sites and, thus, giving high onset potentials and current densities.[47] Pore distribution examined by BJH adsorption method (**Figure 7B**) depicted mesopores sized ~8 nm on Fe/Urea/RGO and ~3 nm on Fe/ChoCl/RGO. Nonetheless, the macropore sized >20 nm caused a slow mass transport on catalytic reaction and thus lowered the ORR performance on Fe/Pani/RGO.[48]

XPS analysis was conducted to explain the role of the inserted metal and heteroatom doped for ORR activity. **Figure 8 and Table** 1 show the survey scan spectra and deconvoluted data, respectively, for all three Fe/X/RGO samples. The deconvoluted spectra of the narrow scans for all samples are presented in the Supporting Information. All samples showed a high composition of carbon and oxygen on the surface.

In general, the C 1s spectra displayed a distinctive single peak rather than the doublet peaks, as observed in other work.[49] This result supports our earlier statement that the GO produced from Sengon wood has undergone the removal of oxygen groups during pyrolysis with metal and nitrogen doping. The deconvoluted spectra represent peaks of C 1s as follows: 284.3 eV for the C-C bond, 284.7 for the C⍰N bond, and 285.7 eV for the C-O bond, which is also assigned to

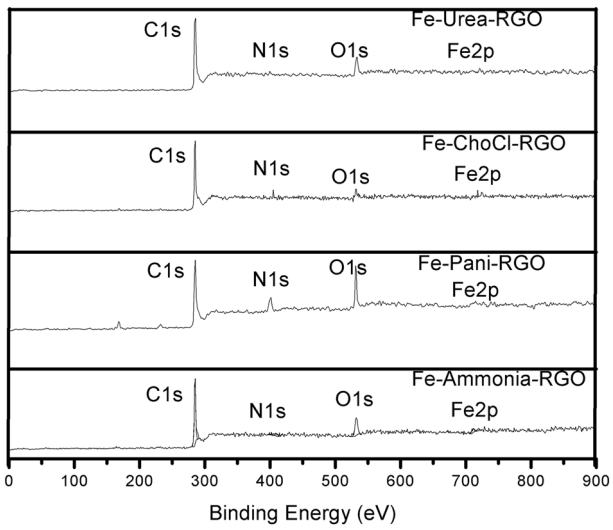

FIGURE 8 XPS survey scan for Fe/Urea/RGO, Fe/ChoCl/RGO, and Fe/Pani/RGO

sp^2 and sp^3 bonding on the graphitic lattice. The C⍰N bond also confirmed the presence of N doping into the carbon matrix. The XPS spectra revealed a significant difference in the oxygen content of each catalyst, with values of 23.37, 11.53, and 30.69 wt% in Fe/Urea/RGO, Fe/ChoCl/RGO, and Fe/Pani/RGO, respectively. A higher oxygen content has been implied to decrease the binding energy between the metal centre and the incoming oxygen molecules as the reactant during the oxygen reduction process, therefore resulting in a slower kinetic reaction and a decrease in the ORR activity in the Fe/Urea/RGO and Fe/Pani/RGO samples.[50] The oxygen bonding nature was further analysed by the O 1s narrow scan. The presence of C⍰O at 531 eV, C-O at 532.1 eV, and C-OH at 533 eV corresponds to the carboxyl group from the RGO Sengon wood functional group, as observed in all samples.[51] In addition, the metal oxide group was also confirmed as an Fe-O bond at 533.7 eV, which corresponded to the detection of Fe_3O_4 in the XRD spectra.

Oxygen reduction on metal-based catalysts theoretically occurred between adjacent metal and nitrogen atom binding active sites.[52] Herein, the iron and nitrogen chemical states were analysed to correlate them with the active sites for ORR activity. The resulting deconvoluted peaks for the Fe 2p peak indicate a pair of Fe bonds with the valence state of Fe^{2+}/Fe^{3+} on the catalyst.[53] However, Fe 2p did not appear clearly on the surface scan due to the low attenuation length and small content incorporated into the carbon matrix.[50]

The pairing peaks at 711.9 and 725.5 eV are attributed to Fe^{2+} 2p, which is present on Fe/N/RGO.[54,55] Satellite peaks at 719 eV indicate the background spectra of Fe_3O_4 formation.[56] Thus, both Fe^{3+} and the background spectra confirm a dominant oxide form, Fe-O, of iron metal on the RGO surface. This finding also agrees with the XRD spectra and the aforementioned O 1s deconvolution peak, which mostly showed a Fe_3O_4 peak on the catalyst. Apart from the bulky agglomerated surface, the oxide functional group apparently decreased the charge density between active sites, which is indicated by positive shift in the binding energy (higher than 2 eV) of Fe 2p from other work (710 eV).[54] It is worth noting that the absence of peaks at 707 eV implies successful leaching of the Fe^0 state or Fe particle during acid washing[47]

The observed N doping deconvoluted peak indicates the type of nitrogen doping on the surface. As presented in Table 1, the polymeric source used to produce Fe/Pani/RGO contained a large amount of nitrogen doped (17.29 at%) on a thick layer on the surface. In contrast,

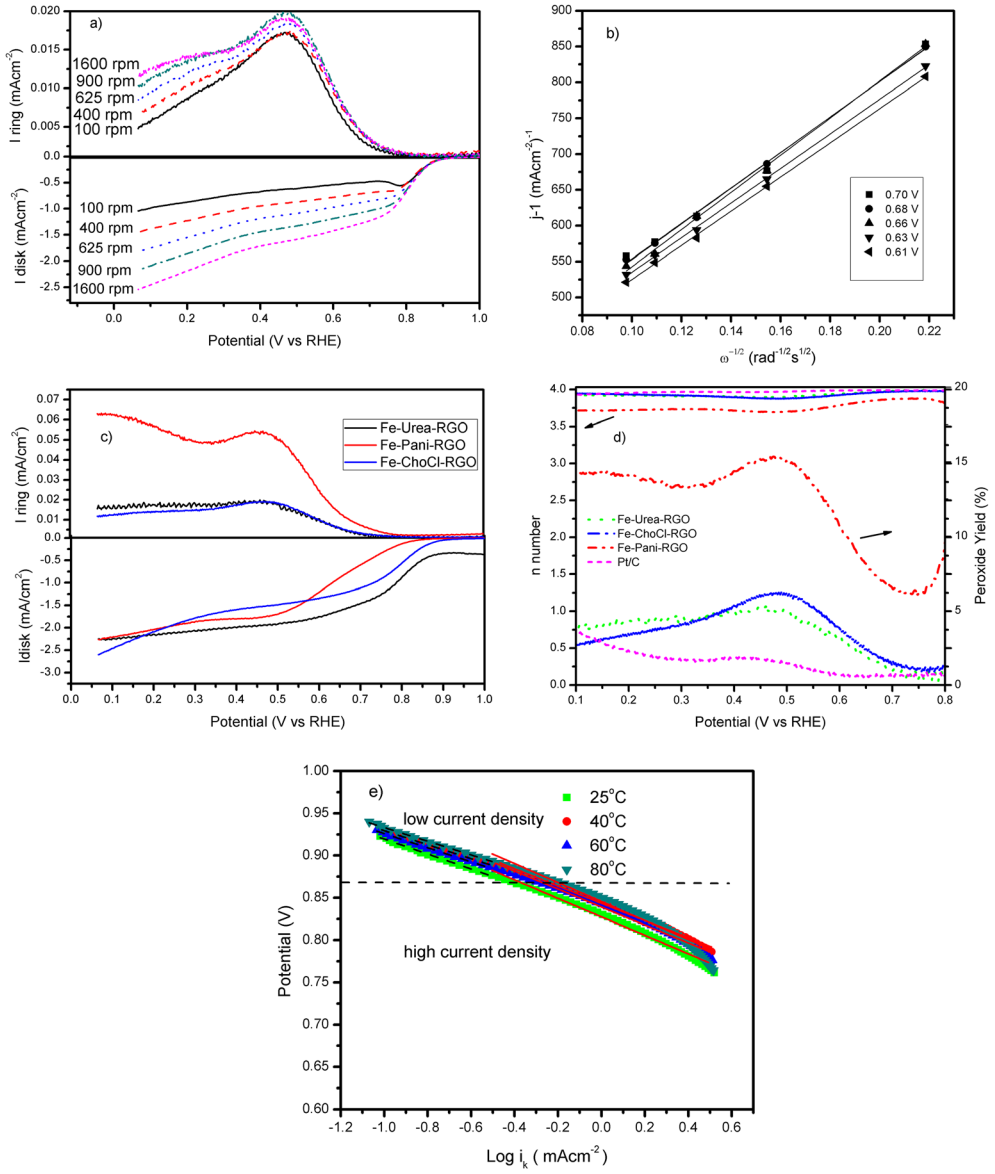

FIGURE 9 (A) Linear sweep voltammogram of Fe/ChoCl/RGO, (B) Koutecky-Levich (K-L) plot, and (C) I disk and I ring for RRDE calculation, (D) n number based on RRDE and H_2O_2 percentages, and (E) Tafel plot on temperature range 25°C to 80°C on Fe/ChoCl/RGO

Fe/ChoCl/RGO and Fe/Urea/RGO had relatively small amounts of nitrogen (3.97 at% and 2.36 at%, respectively) despite their better ORR activity demonstrated in alkaline media. This is an interesting observation, and we can postulate that the nitrogen dopant is not the main determining factor for improved ORR activity. To understand further, we analysed the nitrogen bonding states in each sample (as shown in Table 1).

The deconvoluted peaks were fitted as pyridinic N at 398.9 eV, pyrrolic N at 400 eV, and graphitic N 401 eV, and later, the integrated peaks were calculated as atomic concentrations using CasaXPS software. Among all samples, Fe/ChoCl/RGO displayed the highest percentage of graphitic N in the N 1s spectra with the lowest amount of pyrrolic N, while Fe/Urea/RGO showed a relatively high graphitic N percentage compared with Fe/Pani/RGO, which reported a major percentage of pyrrolic N instead of graphitic N. This observation is believed to be correlated to the surface morphology of the samples, as displayed in **Figure 5A-5C**. The formation of a graphene sheet-like structure with little agglomeration contributed to the high percentage of graphitic N on Fe/ChoCl/RGO; in contrast, a very low percentage of graphitic N in Fe/Pani/RGO reflected its particles with a high degree of agglomeration, indicating the unsuccessful formation of the desired graphitic N or pyridinic N states. It is a common consensus that both pyridinic N and graphitic N are responsible for improving the onset potential and limiting current density, respectively. In this work, we confirmed that pyridinic N and graphitic N both contribute significantly to the ORR activity based on the XPS spectra for the three samples, yet the contribution of each type of bonding state is vague. This is attributed to the presence of Fe in the catalysts, which is believed to have created a synergistic effect with the doped nitrogen, which could be in the form of Fe-Nx,[57,58] that is responsible for contributing to the improvement in the overall ORR activity. It is believed that the synergetic content would be favourable for increasing the mass transfer and oxygen binding on the active sites of the catalysts.

The determination of the electron transfer number was further performed via linear sweep voltammetry at different rotating speeds.

TABLE 2 Comparison on the ORR activity of Fe/X/RGO (X = Pani, Urea, ChoCl) with literature works

Catalysts	Onset Potential, E_{onset} (V vs RHE)	Half Wave Potential, $E_{1/2}$ (V vs RHE)	Current Density ($mAcm^{-1}$ vs RHE)	n	Reference
Soybean carbon doped with Fe and carbon	0.84	0.68	2.18	3.1	[61]
Co/M-chlorella-900	0.84	0.87 V	5.06	4	[62]
Sewage sludge doped with Fe and montmorillonite	0.90	0.89	2.38	3.6	[63]
Pomelo peel in cobalt and nitrogen doped	0.87	0.78	5	3.90	[64]
Fe/Pani/RGO from Sengon Wood	0.87	0.70	2.084	3.77	This work
Fe/Urea/RGO from Sengon Wood	0.89	0.81	2.22	3.93	This work
Fe/ChoCl/RGO from Sengon Wood	0.91	0.84	2.43	3.92	This work

Figure 9A shows the voltammograms of Fe/ChoCl/RGO catalysts at different rotation speeds ranging from 200 to 1600 rpm in 0.1 M KOH under saturated O_2 conditions. The current density curves were shown to increase with higher rotation speeds, indicating a decreased dependence on mass transfer and diffusion factors.[57] The electron transfer number of the Fe/ChoCl/RGO catalyst was extracted via RDE analysis. The Koutecky-Levich plot (K-L) was obtained from Equation (1) and is shown in **Figure 9B** for the low overpotential/kinetic region (0.5-0.7 V vs RHE). The K-L plot results in a number of electron transfers of 3.92, which also agrees with the RRDE calculation (refer to Equation (2) and **Figure 9D)**.

Furthermore, the calculated electron transfers for Fe/Urea/RGO and Fe/Pani/RGO from the RRDE analysis, as presented in **Figure 9C, D**, are 3.93 and 3.77, respectively. These results are closely correlated to the morphology and elemental bonding states in each sample. A lower electron transfer number is noted in Fe/Pani/RGO due to the high degree of particle agglomeration on the surface with the undesired high oxygen content and nitrogen bonding states observed on its surface. Nonetheless, it is worth noting that all samples presented a near four-electron transfer process, indicating a dominant four-electron transfer pathway on all catalysts, denoting the production of H_2O as the final product. Both Fe/ChoCl/RGO and Fe/Urea/RGO samples displayed a low peroxide yield of only ca. 5% during the process, similar to that on Pt/C.

Temperature dependency of the ORR kinetic of Fe/ChoCl/RGO was further studied in the range of 25°C to 80°C to identify its applicability as the cathodic catalyst for fuel cell. Figure 9E displayed the Tafel plots of Fe/ChoCl/RGO obtained at different LSV temperatures. From the calculation, the kinetic transfer coefficient (α) showed the values within 0.32 to 0.35 at low current density region (1.0-0.96 V vs RHE) and increased as 0.45 to 0.51 at high current density (0.9-0.8 V vs RHE). Tafel slope was shown to vary between 88 and 81 mV/dec in the studied temperatures, demonstrating a near to one-electron transfer as rate-determining step despite its more sluggish kinetic than Pt/C. Meanwhile, at the hcd region, the Fe/ChoCl/RGO catalyst has contributed to a less depressed Tafel slope in the range of 101 to 124 mV/dec as compared with Pt/C, 120 mV/dec. The exchange current density was found to be 1.37×10^{-5} to 5.23×10^{-6} mA/cm^2 and assigned for similar order to benchmark Pt/C. This catalyst has evidently shown to be stable kinetically over the temperature range studied and would be suitable for low temperature fuel cell application. Nonetheless, further optimisation would be required to ensure the homogeneity of the catalyst's active sites to ensure a uniform mass transport of reactants during the operation.

The comparison of the results with literature work is shown in **Table** 2. It can be concluded that the RGO from Sengon wood has great potential to act as a catalyst support for respective nitrogen sources through a one-pot synthesis. Therefore, low-cost, noble-free ORR catalysts can be achieved for alkaline fuel cell applications upon further optimisation based on the catalysts and RGO composition.

Chronoamperometry test of Fe/ChoCl/RGO was performed and compared with Pt/C for 16 000 seconds, as depicted in **Figure 10A**. The study showed that the current density of Fe/ChoCl/RGO has retained 85% of its initial value at the applied potential of 0.78 V vs

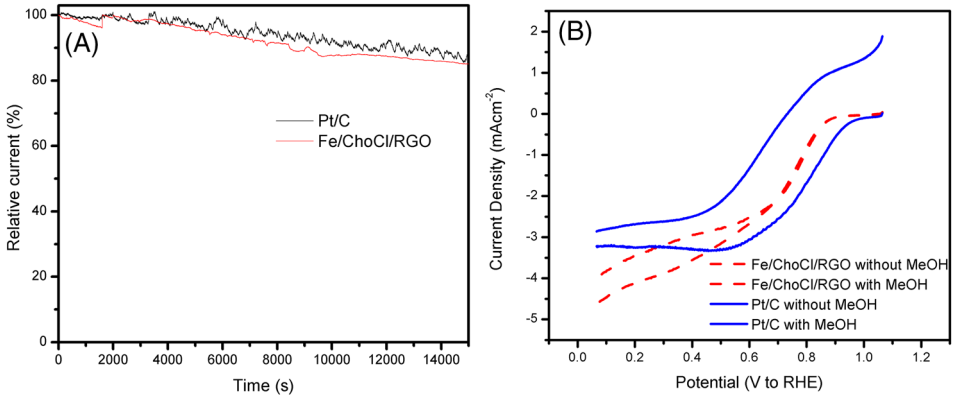

FIGURE 10 (A) Chrono amperometry test of Fe/ChoCl/RGO during 16 000 seconds with O_2 condition; (B) LSV curve of Fe/ChoCl/RGO with and without addition of 3 M methanol (6 mL)

RHE. This result was encouraging as there is only a minor difference in its efficiency as compared with that on Pt/C. We believed that the surface area of Fe/ChoCl/RGO has inhibited active sites degradation during catalytic reaction on long-term usage. However, the result was lower than other iron-based catalyst supported by commercial carbon sources which mostly had less than 10%.[42,59] Methanol fuel crossover was further examined to identify its other application on liquid-based fuel cell (**Figure 10B**). 3 M methanol (6 mL) was injected after 200-second running on 0.1 M KOH solution. A significant 0.12-V onset decay was observed on Pt/C, reducing from 0.96 into 0.84 V vs RHE and half wave potential difference ($\Delta E_{1/2}$) of 0.23 V, affected by vigorous adsorption of methanol and oxygen on catalyst interface. Interestingly, on Fe/ChoCl/RGO, it was observed that only approximately 0.03 V was shifted negatively from the initial onset potential with a 10-mV difference on half wave potential ($\Delta E_{1/2}$), thus signifying a superior methanol resistance on catalyst surface due to RGO mesopores structure.[60]

4 | CONCLUSION

In conclusion, our new approach using the Hummer's method and thermal reduction successfully converted Sengon wood biomass into RGO. The defective nature of the biomass RGO was also shown to demonstrate great potential as an active carbon support for noble-free Fe-N-C catalysts. In this work, it was demonstrated that the thermal reduction of Sengon wood biomass after the Hummer's method at 900°C was most effective in producing RGO with sheet-like structures and many defect sites, low oxygen content, and a high degree of graphitisation, which are desired for a catalyst support. The attempt to anchor noble-free iron/nitrogen/carbon catalysts on the RGO surface via a one-pot synthesis was successful in producing catalysts that are ORR active in alkaline media. Fe/ChoCl/RGO and Fe/Urea/RGO showed electron transfer numbers of 3.92 and 3.93, respectively. In addition, onset and half wave potentials comparable to Pt/C (0.97 V, 0.87 V) were obtained on both samples. Comparable current efficiency through the stability test and better methanol resistant than Pt/C was observed on the Fe/ChoCl/RGO. This shows that low-cost, noble-free metal Fe-N-C catalysts with the employment of naturally abundant Sengon wood biomass sources have the potential to replace scarce and expensive Pt/C as the cathode.

ACKNOWLEDGEMENT

The authors would like to acknowledge financial support from the Universiti Kebangsaan Malaysia through the project GUP-2018-013. The authors would also like to thank Nuclear Malaysia for providing FESEM, Raman, and XRD facilities for the characterizations, Synchotron Light Research Institute (SLRI) Thailand for providing XPS characterization, and the Center of Research and Instrumentation (CRIM) UKM for the TEM analysis.

ORCID

Wai Yin Wong https://orcid.org/0000-0002-5093-1431

REFERENCES

1. Liang X, Liu W, Cheng Y, et al. Review: Recent process in the design of carbon-based nanostructures with optimized electromagnetic properties. *J Alloys Compd*. 2018;749:887-899.
2. Borup KA, de Boor J, Wang H, et al. Measuring thermoelectric transport properties of materials. *Energ Environ Sci*. 2015;8(2):423-435.
3. Liu J, Takeshi D, Orejon D, Sasaki K, Lyth SM. Defective nitrogen-doped graphene foam: a metal-free, non-precious electrocatalyst for the oxygen reduction reaction in acid. *J Electrochem Soc*. 2014;161(4):F544-F550.
4. Karim NA, Kamarudin SK, Shyuan LK, Yaakob Z, Daud WRW, Kadhum AAH. Study on the electronic properties and molecule adsorption of W18O49 nanowires as a catalyst support in the cathodes of direct methanol fuel cells. *J Power Sources*. 2015;288:461-472.
5. Zainul Abidin AF, Loh KS, Wong WY, Mohamad AB, Puspasari I. Effect of carbon precursor and initial pH on cobalt-doped carbon xerogel for oxygen reduction. *Int J Hydrogen Energy*. 2018;43(24):11047-11055.
6. Liu J, Deng Y, Li X, Wang L. Promising nitrogen-rich porous carbons derived from one-step calcium chloride activation of biomass-based waste for high performance supercapacitors. *ACS Sustain Chem Eng*. 2016;4(1):177-187.
7. Memioğlu F, Bayrakçeken A, Öznülüer T, Ak M. Conducting carbon/-polymer composites as a catalyst support for proton exchange membrane fuel cells. *Int J Energy Res*. 2014;38(10):1278-1287.
8. Fan X, Zhang G, Zhang F. Multiple roles of graphene in heterogeneous catalysis. *Chem Soc Rev*. 2015;44(10):3023-3035.
9. Shams SS, Zhang LS, Hu R, Zhang R, Zhu J. Synthesis of graphene from biomass: a green chemistry approach. *Mater Lett*. 2015;161:476-479.
10. Liu X, Zhang M, Yu D, et al. Functional materials from nature: honeycomb-like carbon nanosheets derived from silk cocoon as excellent electrocatalysts for hydrogen evolution reaction. *Electrochim Acta*. 2016;215:223-230.
11. Purkait T, Singh G, Singh M, Kumar D, Dey RS. Large area few-layer graphene with scalable preparation from waste biomass for high-performance supercapacitor. *Sci Rep*. 2017;7(1):1-14.
12. Ekhlasi L, Younesi H, Rashidi A, Bahramifar N. Populus wood biomass-derived graphene for high CO2 capture at atmospheric pressure and estimated cost of production. *Process Saf Environ Prot*. 2018;113:97-108.
13. Sun Z, Zheng M, Hu H, et al. From biomass wastes to vertically aligned graphene nanosheet arrays: a catalyst-free synthetic strategy towards high-quality graphene for electrochemical energy storage. *Chem Eng J*. 2018;336:550-561.
14. Chen F, Yang J, Bai T, Long B, Zhou X. Facile synthesis of few-layer graphene from biomass waste and its application in lithium ion batteries. *J Electroanal Chem*. 2016;768(Supplement C):18-26.
15. Gewirth AA, Varnell JA, Diascro AM. Nonprecious metal catalysts for oxygen reduction in heterogeneous aqueous systems. *Chem Rev*. 2018;118(5):2313-2339.
16. Shao M, Chang Q, Dodelet J-P, Chenitz R. Recent advances in electrocatalysts for oxygen reduction reaction. *Chem Rev*. 2016;116(6):3594-3657.
17. Osmieri L, Escudero-Cid R, Armandi M, et al. Fe-N/C catalysts for oxygen reduction reaction supported on different carbonaceous materials. Performance in acidic and alkaline direct alcohol fuel cells. *Appl Catal Environ*. 2017;205:637-653.
18. Atta-Obeng E, Dawson-Andoh B, Seehra MS, Geddam U, Poston J, Leisen J. Physico-chemical characterization of carbons produced from technical lignin by sub-critical hydrothermal carbonization. *Biomass Bioenergy*. 2017;107:172-181.
19. Soo LT, Loh KS, Mohamad AB, Daud WRW, Wong WY. Effect of nitrogen precursors on the electrochemical performance of nitrogen-

doped reduced graphene oxide towards oxygen reduction reaction. *J Alloys Compd*. 2016;677:112-120.
20. Wang G, Peng H, Qiao X, et al. Biomass-derived porous heteroatom-doped carbon spheres as a high-performance catalyst for the oxygen reduction reaction. *Int J Hydrogen Energy*. 2016;41(32):14101-14110.
21. Mondal D, Sharma M, Wang C-H, et al. Deep eutectic solvent promoted one step sustainable conversion of fresh seaweed biomass to functionalized graphene as a potential electrocatalyst. *Green Chem*. 2016;18(9):2819-2826.
22. Mitra M, Kulsi C, Chatterjee K, et al. Reduced graphene oxide-polyaniline composites—synthesis, characterization and optimization for thermoelectric applications. *RSC Adv*. 2015;5(39):31039-31048.
23. Guo C, Liao W, Li Z, et al. Coprinus comatus-derived nitrogen-containing biocarbon electrocatalyst with the addition of self-generating graphene-like support for superior oxygen reduction reaction. *Sci Bull*. 2016;61(12):948-958.
24. Song C, Zhang J. Electrocatalytic oxygen reduction reaction. In: *PEM Fuel Cell Electrocatalysts and Catalyst Layers: Fundamentals and Applications*. ; 2008:89-134.
25. Shinagawa T, Garcia-Esparza AT, Takanabe K. Insight on Tafel slopes from a microkinetic analysis of aqueous electrocatalysis for energy conversion. *Sci Rep*. 2015;5(May):1-21.
26. Wong WY, Daud WRW, Mohamad AB, Loh KS. Effect of temperature on the oxygen reduction reaction kinetic at nitrogen-doped carbon nanotubes for fuel cell cathode. *Int J Hydrogen Energy*. 2015;40(35):11444-11450.
27. Sharabi R, Wijsboom YH, Borchtchoukova N, Finkelshtain G, Elbaz L. Methodology for the design of accelerated stress tests for non-precious metal catalysts in fuel cell cathodes. *J Power Sources*. 2016;335:56-64.
28. Luo D, Zhang X. The effect of oxygen–containing functional groups on the H2 adsorption of graphene–based nanomaterials: experiment and theory. *Int J Hydrogen Energy*. 2018;43(11):5668-5679.
29. Zhuang S, Nunna BB, Boscoboinik JA, Lee ES. Nitrogen-doped graphene catalysts: high energy wet ball milling synthesis and characterizations of functional groups and particle size variation with time and speed. *Int J Energy Res*. 2017;41(15):2535-2554.
30. He T-S, Ren X, Wang Y-B, Nie J-P, Cai K-D. Electrochemical performance of reduced graphene oxide in Spiro-(1, 1')-bipyrrolidinium tetrafluoroborate electrolyte. *Int J Energy Res*. 2016;40(8):1105-1111.
31. Vazquez-Moreno JM, Yuste-Sanchez V, Sanchez-Hidalgo R, et al. Customizing thermally-reduced graphene oxides for electrically conductive or mechanical reinforced epoxy nanocomposites. *Eur Polym J*. 2017;93:1-7.
32. Amiinu IS, Zhang J, Kou Z, et al. Self-organized 3D porous graphene dual-doped with biomass-sponsored nitrogen and sulfur for oxygen reduction and evolution. *ACS Appl Mater Interfaces*. 2016;8(43):29408-29418.
33. Jha PK, Singh SK, Kumar V, Rana S, Kurungot S, Ballav N. High-level supercapacitive performance of chemically reduced graphene oxide. *Chem*. 2017;3(5):846-860.
34. Schöche S, Hong N, Khorasaninejad M, et al. Optical properties of graphene oxide and reduced graphene oxide determined by spectroscopic ellipsometry. *Appl Surf Sci*. 2017;421:778-782.
35. Dimiev AM, Alemany LB, Tour JM. Graphene oxide. origin of acidity, its instability in water, and a new dynamic structural model. *ACS Nano*. 2013;7(1):576-588.
36. Antolini E. Graphene as a new carbon support for low-temperature fuel cell catalysts. *Appl Catal Environ*. 2012;123:52-68.
37. Wu W, Leng J, Mei H, Yang S. Defect-rich, boron-nitrogen bonds-free and dual-doped graphenes for highly efficient oxygen reduction reaction. *J Colloid Interface Sci*. 2018;521:11-16.
38. Fromm O, Heckmann A, Rodehorst UC, et al. Carbons from biomass precursors as anode materials for lithium ion batteries: new insights into carbonization and graphitization behavior and into their correlation to electrochemical performance. *Carbon*. 2018;128:147-163.
39. Fan W, Zhang C, Tjiu WW, Pramoda KP, He C, Liu T. Graphene-wrapped polyaniline hollow spheres as novel hybrid electrode materials for supercapacitor applications. *ACS Appl Mater Interfaces*. 2013;5(8):3382-3391.
40. Wang HF, Tang C, Wang B, Li BQ, Cui X, Zhang Q. Defect-rich carbon fiber electrocatalysts with porous graphene skin for flexible solid-state zinc–air batteries. *Energy Storage Mater*. 2018;15:124-130.
41. Hu H, Liu R, Si S, Kong D, Feng Y. Iron and nitrogen codoped carbon catalyst with excellent stability and methanol tolerance for oxygen reduction reaction. *Int J Energy Res*. 2019;43(13):7107-7119.
42. Li JC, Tang DM, Hou PX, et al. The effect of carbon support on the oxygen reduction activity and durability of single-atom iron catalysts. *MRS Commun*. 2018;8(3):1158-1166.
43. Jiao Y, Zheng Y, Jaroniec M, Qiao SZ. Origin of the electrocatalytic oxygen reduction activity of graphene-based catalysts: a roadmap to achieve the best performance. *J Am Chem Soc*. 2014;136(11):4394-4403.
44. Chen N, Ren Y, Kong P, Tan L, Feng H, Luo Y. In situ one-pot preparation of reduced graphene oxide/polyaniline composite for high-performance electrochemical capacitors. *Appl Surf Sci*. 2017;392:71-79.
45. Sun J, Niu J, Liu M, Ji J, Dou M, Wang F. Biomass-derived nitrogen-doped porous carbons with tailored hierarchical porosity and high specific surface area for high energy and power density supercapacitors. *Appl Surf Sci*. 2018;427:807-813.
46. Demir M, Ashourirad B, Mugumya JH, Saraswat SK, El-kaderi HM, Gupta RB. Nitrogen and oxygen dual-doped porous carbons prepared from pea protein as electrode materials for high performance supercapacitors. *Int J Hydrogen Energy*. 2018;43(40):18549-18558.
47. Tang F, Lei H, Wang S, Wang H, Jin Z. A novel Fe–N–C catalyst for efficient oxygen reduction reaction based on polydopamine nanotubes. *Nanoscale*. 2017;9(44):17364-17370.
48. Hou J, Liu Z, Yang S, Zhou Y. Three-dimensional macroporous anodes based on stainless steel fiber felt for high-performance microbial fuel cells. *J Power Sources*. 2014;258:204-209.
49. Molina-García MA, Rees NV. Effect of catalyst carbon supports on the oxygen reduction reaction in alkaline media: a comparative study. *RSC Adv*. 2016;6(97):94669-94681.
50. Artyushkova K, Matanovic I, Halevi B, Atanassov P. Oxygen binding to active sites of Fe-N-C ORR electrocatalysts observed by ambient-pressure XPS. *J Phys Chem C*. 2017;121(5):2836-2843.
51. Liu B, Yang M, Yang D, Chen H, Li H. Medulla tetrapanacis-derived O/N co-doped porous carbon materials for efficient oxygen reduction electrocatalysts and high-rate supercapacitors. *Electrochim Acta*. 2018;272:88-96.
52. Artyushkova K, Matanovic I, Chen Y, Atanassov P, Weiler E. Mechanism of oxygen reduction reaction on transition metal–nitrogen–carbon catalysts: establishing the role of nitrogen-containing active sites. *ACS Appl Energy Mater*. 2018;1(11):5948-5953.
53. Chung MW, Choi CH. Carbon nanofibers as parent materials for a graphene-based Fe-N-C catalyst for the oxygen reduction reaction. *Catal Today*. 2017;295:125-131.
54. Ren G, Gao L, Teng C, et al. Ancient chemistry "pharaoh's snakes" for efficient Fe-/N-doped carbon electrocatalysts. *ACS Appl Mater Interfaces*. 2018;10(13):10778-10785.
55. Xu X, Shi C, Li Q, Chen R, Chen T. Fe-N-Doped carbon foam nanosheets with embedded Fe2O3nanoparticles for highly efficient oxygen reduction in both alkaline and acidic media. *RSC Adv*. 2017;7(24):14382-14388.
56. Domínguez C, Pérez-Alonso FJ, Salam MA, et al. Repercussion of the carbon matrix for the activity and stability of Fe/N/C electrocatalysts for the oxygen reduction reaction. *Appl Catal Environ*. 2016;183:185-196.

57. Monteverde Videla AHA, Ban S, Specchia S, Zhang L, Zhang J. Non-noble Fe-NX electrocatalysts supported on the reduced graphene oxide for oxygen reduction reaction. *Carbon N Y*. 2014;76:386-400.
58. Ma R, Ren X, Xia BY, et al. Novel synthesis of N-doped graphene as an efficient electrocatalyst towards oxygen reduction. *Nano Res*. 2016;9(3):808-819.
59. Liu Y, Ruan J, Sang S, Zhou Z, Wu Q. Iron and nitrogen co-doped carbon derived from soybeans as efficient electro-catalysts for the oxygen reduction reaction. *Electrochim Acta*. 2016;215:388-397.
60. Gu L, Jiang L, Li X, Jin J, Wang J, Sun G. A Fe-N-C catalyst with highly dispersed iron in carbon for oxygen reduction reaction and its application in direct methanol fuel cells. *Cuihua Xuebao/Chinese J Catal*. 2016;37(4):539-548.
61. Guo CZ, Liao WL, Chen CG. Design of a non-precious metal electrocatalyst for alkaline electrolyte oxygen reduction by using soybean biomass as the nitrogen source of electrocatalytically active center structures. *J Power Sources*. 2014;269:841-847.
62. Wang G, Deng Y, Yu J, et al. From Chlorella to nestlike framework constructed with doped carbon nanotubes: a biomass-derived, high-performance, bifunctional oxygen reduction/evolution catalyst. *ACS Appl Mater Interfaces*. 2017;9(37):32168-32178.
63. Chen M, Wu P, Chen L, et al. Three-dimensional multi-doped porous carbon/graphene derived from sewage sludge with template-assisted fe-pillared montmorillonite for enhanced oxygen reduction reaction. *Sci Rep*. 2017;7(1):1-10.
64. Zhang M, Jin X, Wang L, et al. Improving biomass-derived carbon by activation with nitrogen and cobalt for supercapacitors and oxygen reduction reaction. *Appl Surf Sci*. 2017;411:251-260.

How to cite this article: Sudarsono W, Wong WY, Loh KS, et al. Noble-free oxygen reduction reaction catalyst supported on Sengon wood (*Paraserianthes falcataria L.*) derived reduced graphene oxide for fuel cell application. *Int J Energy Res*. 2019; 1–14. https://doi.org/10.1002/er.5015